

An Experimental Study of Loss Sources in a Fan Operating With Continuous Inlet Stagnation Pressure Distortion

Ewan J. Gunn
e-mail: ejg55@cam.ac.uk

Sarah E. Tooze

Cesare A. Hall

Yann Colin

Whittle Laboratory,
University of Cambridge,
1 JJ Thomson Avenue,
Cambridge CB3 0DY, UK

The viability of boundary layer ingesting (BLI) engines for future aircraft propulsion is dependent on the ability to design robust, efficient engine fan systems for operation with continuously distorted inlet flow. A key step in this process is to develop an understanding of the specific mechanisms by which an inlet distortion affects the performance of a fan stage. In this paper, detailed full-annulus experimental measurements of the flow field within a low-speed fan stage operating with a continuous 60 deg inlet stagnation pressure distortion are presented. These results are used to describe the three-dimensional fluid mechanics governing the interaction between the fan and the distortion and to make a quantitative assessment of the impact on loss generation within the fan. A 5.3 percentage point reduction in stage total-to-total efficiency is observed as a result of the inlet distortion. The reduction in performance is shown to be dominated by increased loss generation in the rotor due to off-design incidence values at its leading edge, an effect that occurs throughout the annulus despite the localized nature of the inlet distortion. Increased loss in the stator row is also observed due to flow separations that are shown to be caused by whirl angle distortion at rotor exit. By addressing these losses, it should be possible to achieve improved efficiency in BLI fan systems. [DOI: 10.1115/1.4007835]

Introduction

Boundary layer ingesting (BLI) engines have the potential to offer significant reductions in fuel burn compared with traditional podded turbofans. These engines would rely on similar high-bypass turbofan technology to the engines of today, but they would be positioned on the airframe such that their intakes capture a significant portion of the airframe boundary layer fluid. The ingestion of this boundary layer fluid leads to a reduction in the wasted kinetic energy associated with the wake of the aircraft [1]. The lack of pylon supports and the ability to blend the engine intakes into the airframe also lead to reductions in installation weight, viscous drag and ram drag compared with podded turbofans [2]. Because of these benefits, BLI engines have been repeatedly identified as a key technology in various concept aircraft studies [3–7]. Predictions of the fuel burn reductions attributable to their use typically range from around 5% to 15% relative to otherwise identical airframes using podded turbofans [4,7,8].

However, the challenge of turbomachinery design for BLI is yet to be addressed. By definition a BLI intake will deliver flow with nonuniform, or “distorted,” stagnation pressure and velocity to the engine fan. Although various studies [8–12] have demonstrated that BLI intakes can be optimized using passive or active means to help reduce distortion transfer to the engine, it cannot be eliminated. For BLI technology to be viable, engine fans that can operate efficiently and reliably with continuously distorted inlet flow conditions are required.

Previous studies have found that the aerodynamic performance of fans and compressors, in terms of efficiency and pressure rise, is detrimentally affected by the introduction of inlet stagnation pressure or swirl distortion and the consequent flow nonuniformity; reviews of much of this work can be found in [13] and [14]. Stability is reduced and work has been done on characterizing the

severity of general inlet distortion patterns, allowing models and correlations to be used to estimate the reduction in stability [13–16]. Flow field coupling has also been found to become more pronounced when inlet distortion is introduced [14,17,18]. This includes coupling between compressor components as well as coupling of components to the inlet flow field and downstream features.

In recent years, the understanding of fan-distortion interaction has been advanced by various computational studies utilizing three-dimensional, unsteady, full-annulus CFD calculations. A three-stage fan with a sinusoidal inlet stagnation pressure distortion was studied in [19,20], demonstrating the ability of such calculations to capture the distortion transfer through the stages. In [21], the flow through a transonic fan operating with a 120 deg sector inlet stagnation pressure distortion was computed. The results showed how the fan rotor redistributed the upstream flow and revealed details of the distortion transfer and component coupling within the stage.

Experimental studies of fan performance with inlet distortion have been carried out for several decades, focusing mainly on military configurations [22–27]. However, conventional tests of fans operating with inlet distortion typically have limited measurement resolution. The instrumentation is generally sufficient to characterize the distortion and to measure overall performance, but unable to resolve three-dimensional flow features or coupling effects. In this paper, high-resolution, full-annulus measurements are presented that fully resolve the 3D flow features generated by the interaction of a distortion with a single-stage, low hub-to-tip ratio fan. The objectives are to use these measurements to understand the resulting flow field and to determine how the inlet distortion leads to the generation of additional loss in the rotor and stator.

The approach taken is to first describe the overall performance of a new single-stage, low-speed fan rig operating with a continuous, uniform, 60 deg sector inlet stagnation pressure distortion. Although this pattern does not represent a practical BLI inlet flow, its simplicity allows the important flow physics to be readily

Contributed by the International Gas Turbine Institute (IGTI) of ASME for publication in the JOURNAL OF TURBOMACHINERY. Manuscript received July 17, 2012; final manuscript received September 3, 2012; published online June 24, 2013. Editor: David Wisler.

identified. Full-annulus, high spatial resolution measurements of the flow field are then presented and used to develop an understanding of the fluid mechanics governing the upstream fan-distortion interaction and the distortion transfer, demonstrating the development of three-dimensional flow features that persist through the stage. The performance of the fan is then analyzed quantitatively and compared with its performance in clean flow. A new method is applied to the measured data to track fluid from rotor inlet to rotor exit so that the performance of individual rotor sectors can be estimated. These analyses are combined with the understanding of the flow field to develop specific explanations of the mechanisms by which the inlet distortion leads to the generation of additional loss in the fan.

Experimental Methods

The experimental rig employed for the research is a new low-speed, single-stage fan, which has been purpose-built to enable the measurement of BLI-related effects on fan performance. It is shown schematically in Fig. 1 and its main parameters are summarized in Table 1.

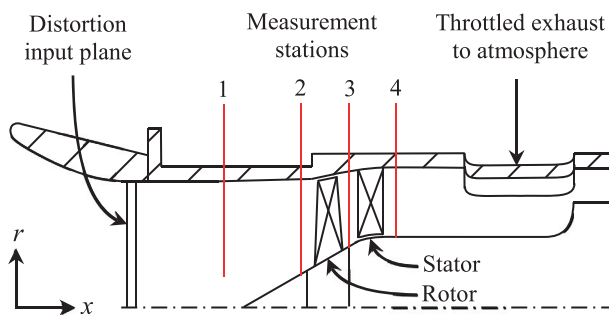


Fig. 1 Meridional view of the rig, to scale

Table 1 Rig geometry and design point performance parameters

Flow coefficient	0.50
Stage loading coefficient	0.47
Stage reaction	0.81
Rotor inlet tip relative Mach number	0.13
Rotor inlet hub-to-tip radii ratio	0.30
Rotor inlet tip diameter (m)	0.47
Number of rotor blades	20
Number of stator blades	30

The rotor blade geometry is similar to that which would be used in a transonic fan. Figure 2 illustrates this by comparing three representative sections from the present rig and the NASA Rotor 67 [28]. In a transonic fan, flow turning towards the low-camber blade tip sections is accomplished through deceleration of the flow in the relative frame by shocks. Although the low-speed test rig is unable to match these and other compressible flow features, or to match their interaction with the inlet distortion, the spanwise distributions of work and loss in the low-speed rotor have been designed to approximately resemble those of a transonic rotor at the design point. This was accomplished by adjusting the low-speed rotor blades such that the sections near the tip operate at positive incidence. This incidence generates additional flow turning and loss, which in a transonic fan would be generated by shocks.

Pitot tubes and static pressure taps at station 1 were used to measure the mass flow rate through the rig, which was controlled using a throttle downstream of the stage. Static pressure taps at the remaining stations were used to measure total-to-static pres-

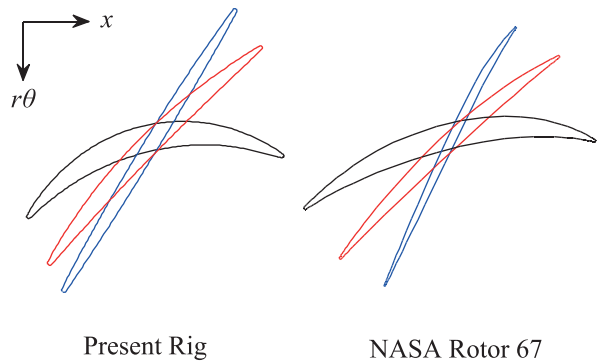


Fig. 2 Comparison of rotor blade sections for the present rig and NASA Rotor 67 [28]. Hub, midspan, and tip are shown in black, red, and blue, respectively.

sure rise characteristics for the machine. These were complemented by a tachometer and torque meter connected to the drive motor, which were used to measure the total work input to the rotor and hence allow the measurement of total-to-static efficiency characteristics.

Detailed measurements of the flow field were made using a motorized five-hole pressure probe area traverse system. The probe was traversed radially and circumferentially at each of stations 1-4 on a grid of points within a fixed 36 deg sector of the rig, corresponding to three stator blade pitches. Approximately 950 measurements per 36 deg sector were made at each of stations 1-3, while 1900 measurements per 36 deg sector were made at station 4 to enable resolution of the stator blade wakes and end-wall flows. Figure 3 shows the grid of measurement points for a 36 deg sector at station 2. The five-hole probe was calibrated over a full range of whirl and radial angles in a low-speed wind tunnel following the method described in [29]. This calibration enabled stagnation and dynamic pressures together with the flow angles to be accurately determined at each measurement position. The expected errors in these quantities are of the order of 0.8% and 0.5 deg, respectively. The assumption of incompressibility also allowed the three-dimensional velocity field to be calculated from these measurements. Note that no interpolation or smoothing of the measurement data has been carried out in constructing any of the full-annulus plots of the flow field that appear in the following sections.

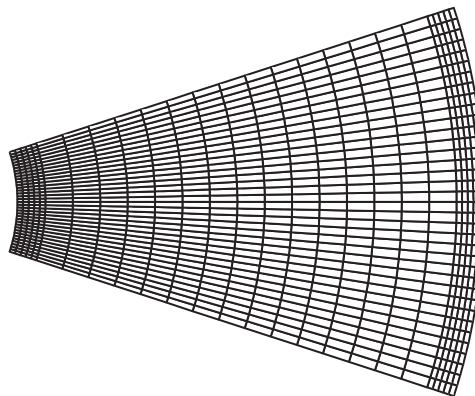


Fig. 3 36 deg sector of the measurement grid at station 2

A stagnation pressure distortion was created in the inlet of the rig by fixing a gauze sector at the location shown on Fig. 1. Figure 4 shows the arrangement considered in this paper, with a single uniform gauze covering a 60 deg sector, leading to a uniform stagnation pressure deficit downstream. An indication of the

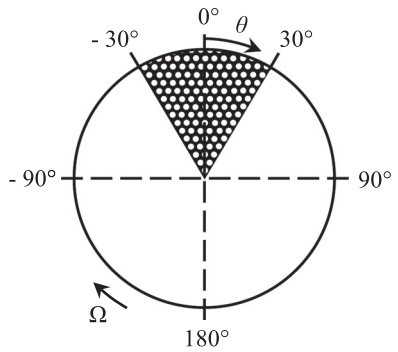
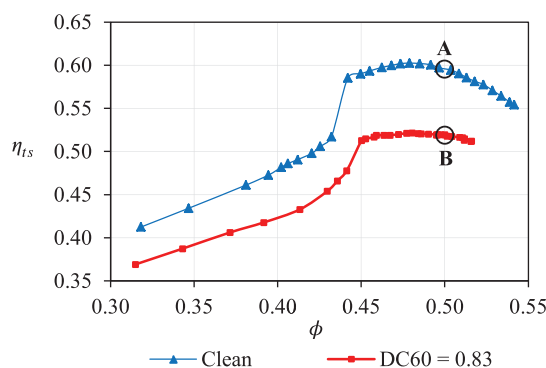
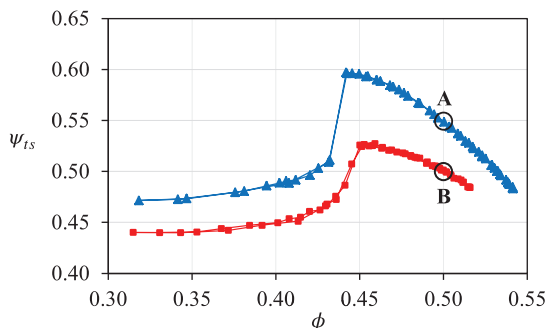


Fig. 4 Schematic view looking into the rig intake with a 60 deg gauze sector in place



A: Design point
B: Operating point for full-annulus traverses in distorted flow

Fig. 5 Stage total-to-static pressure rise and efficiency characteristics at constant rotor speed

intensity of this distortion is given by its DC₆₀ value of 0.83, as defined below [30]

$$DC_{60} = \frac{\overline{P}_{01,360\text{ deg}} - \overline{P}_{01,60\text{ deg}}}{\frac{1}{2}\rho V_1^2} \quad (1)$$

The numerator is the difference between the full-annulus mass-averaged stagnation pressure and the mass-averaged stagnation pressure within the distorted sector, while the denominator is a reference pressure; in this case the average dynamic head. As stated in the Introduction, this uniform sector distortion does not represent the true distortion pattern that would be encountered in a BLI application. However, the resulting flow field allows a clear distinction to be made between the regions of distorted and undistorted flow in the inlet. This makes it easier to identify the origin of flow features that are observed downstream and to analyze the machine's performance. The relatively high intensity of the distortion also makes it easier to measure its effect on the sources of loss within the stage.

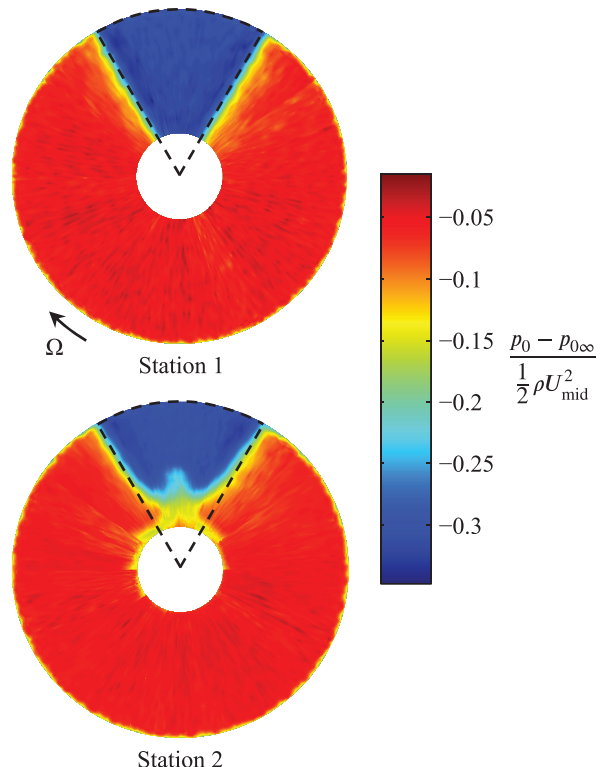


Fig. 6 Contours of stagnation pressure upstream of the rotor

Constant-speed characteristic curves for the rig are shown in Fig. 5. Throughout the operating range of the fan, total-to-static pressure rise and efficiency are reduced with inlet distortion present. Point A on Fig. 5 indicates the design operating point. Full-annulus area traverses with inlet distortion were carried out at point B, corresponding to the same nondimensional mass flow rate as point A, and the results are presented in the following sections. These full-annulus traverses were obtained by carrying out 10 area traverses at each station, with the intake distortion rotated by increments of 36 deg between the runs.

Fan Flow Field With Inlet Distortion

Upstream Flow Redistribution. Figures 6–9 show contour plots of the pressure fields and flow angles upstream of the rotor with the machine operating point fixed at $\phi = 0.5$ and the DC₆₀ = 0.83 gauze in place. The outline of a 60 deg sector, centered at the same position as the gauze in Fig. 4, is superimposed on each plot as a visual reference. All the plots show views looking into the rig using the same coordinate system as Fig. 4. Note that at station 1 the traverse data does not extend all the way to the rig centerline.

The upper plot in Fig. 6 shows that at station 1, midway between the gauze and the rotor, the distortion takes the form of a stagnation pressure deficit of fairly constant magnitude within the 60 deg distorted sector. On the other hand, the static pressure at this station is more uniform (Fig. 7). The result of the stagnation and static pressure profiles at station 1 is that the flow has an axial velocity deficit, which is of essentially the same form as the stagnation pressure deficit. Due to the negative slope of the pressure rise characteristic curve, the fan rotor sucks harder on the slower moving flow in the distorted sector. Low static pressure is induced in this sector as the flow moves downstream and the intensity of this static pressure distortion increases as the flow approaches the rotor leading edge. Figure 7 shows that the static pressure distortion near the rotor leading edge is of the same order of magnitude as the original stagnation pressure distortion.

The circumferential and radial pressure gradients that are produced result in a redistribution of mass flow upstream of the rotor. The pressure gradients act to drive flow from the undistorted portion of the

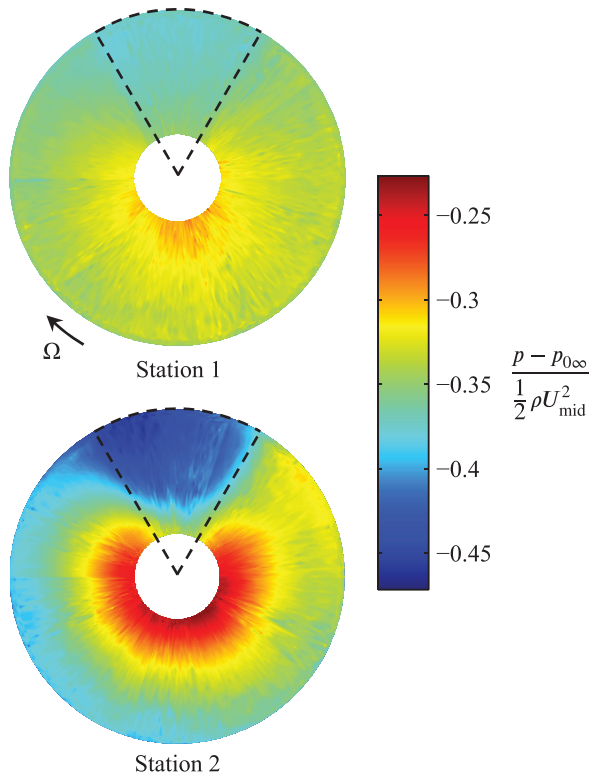


Fig. 7 Contours of static pressure upstream of the rotor

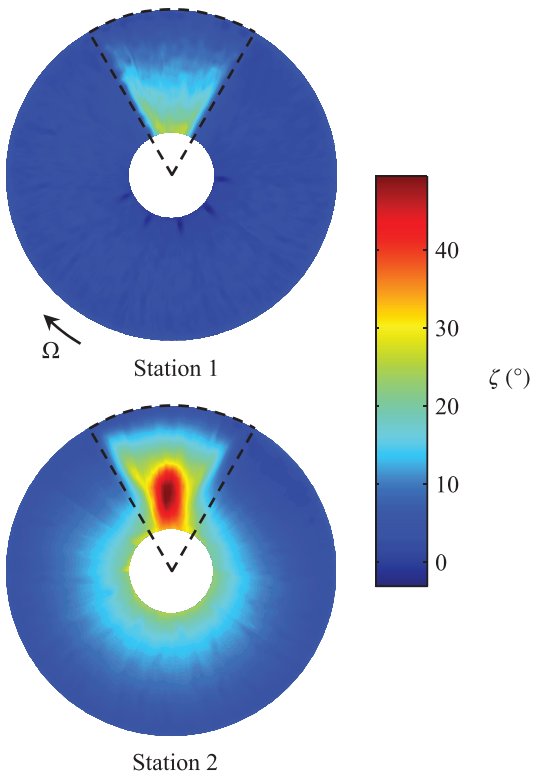


Fig. 9 Contours of radial angle upstream of the rotor

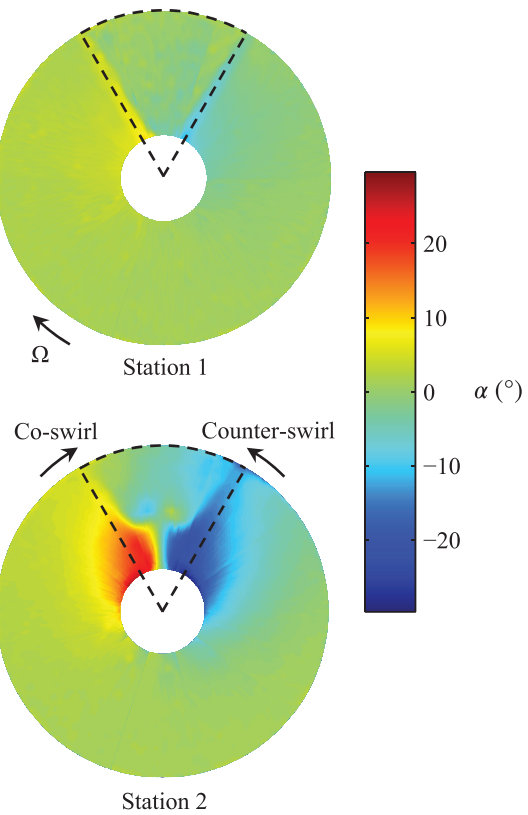


Fig. 8 Contours of absolute whirl angle upstream of the rotor

annulus into the distorted sector, causing a migration of high stagnation pressure fluid into the distorted sector near the hub that can be seen on the bottom of Fig. 6. Figures 8 and 9 show the effect of these pressure gradients on the angularity of the flow.

At station 1, upstream of the spinner, the rate of circumferential migration of fluid is low. Little whirl angle distortion is present on the top of Fig. 8. However, due to the lack of a hub barrier, a radial flow is driven directly across the annulus, as shown on the top of Fig. 9. At station 2, the path directly across the annulus is blocked by the spinner cone. The nature of the redistributing flow changes and it interacts strongly with the spinner. Fluid originating from outside the distorted sector is driven circumferentially around the sides of the spinner, leading to regions of strong co-swirl and counter-swirl near the hub that can be seen on the bottom of Fig. 8. Where these two streams of fluid meet, an intense radial jet, shown on the bottom of Fig. 9, carries the migrating fluid outward from the hub into the distorted sector. Because of the strength of this flow around the spinner, the migration of fluid into the distorted sector mainly occurs close to the hub. However, this migration leads to a redistribution of mass throughout the distorted sector, as the flow in the remainder of the sector is driven outwards towards the casing. Above midspan, little circumferential flow migration takes place and this internal radial flow within the distorted sector is the dominant mechanism for mass redistribution. Figure 6 shows that above midspan, the shear layers bounding the distorted sector move inwards by only a few degrees between stations 1 and 2.

The influx of mass around the spinner and the resulting redistribution of mass in the distorted sector cause the mass flow rate throughout the sector to increase by 50% between stations 1 and 2. This compares to a mean flow acceleration, due to convergence of the annulus, of around 1%–2% between these stations. The flow redistribution therefore results in an attenuation of the axial velocity distortion at the rotor leading edge compared with that upstream. However, the axial velocity distribution at station 2 can be seen on the top of Fig. 10 and this plot shows that the flow coefficient in the distorted sector at the rotor leading edge is around 0.35. This is still well beyond the uniform flow stability boundary observed in Fig. 5. A parallel compressor analysis of this system would therefore predict that stable operation of the fan

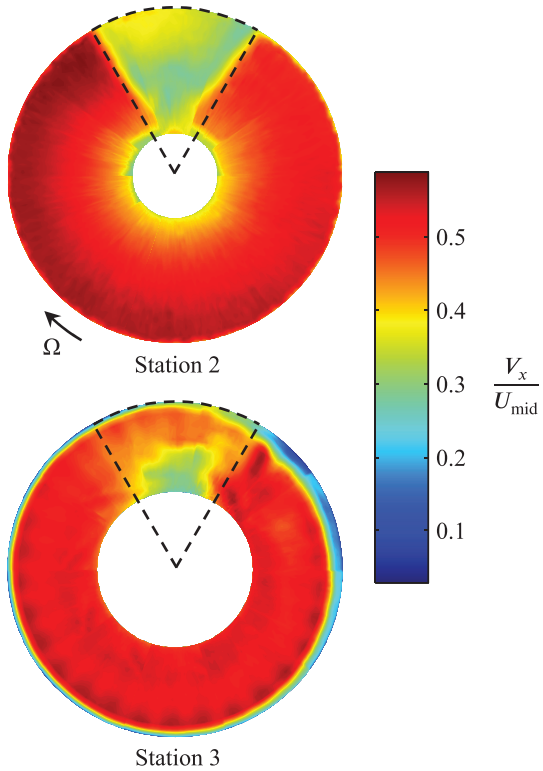


Fig. 10 Contours of axial velocity at rotor inlet and exit

would be impossible with this level of inlet distortion. Further upstream at station 1, the flow coefficient in the distorted sector is even lower at $\phi = 0.23$. The local flow coefficient in this sector is therefore brought closer to the uniform flow stability limit as the rotor leading edge is approached, indicating that the rotor-induced upstream flow redistribution promotes stability. A similar observation was made in [21] for a transonic fan operating with a continuous inlet stagnation pressure distortion.

The dominance of the radial mechanism of flow redistribution distinguishes the problem of distorted flow through low hub-to-tip ratio fans from that through higher hub-to-tip ratio compressors. Any methods used to model these flows will therefore have to be 3D in nature. Full-annulus, unsteady, 3D computational calculations of such flows are now feasible, and the results of such a calculation for a single-stage transonic fan show the development of a similar mass flow redistribution upstream of the rotor [21].

Distortion Transfer Through the Rotor and Stator. The incidence of the flow onto the rotor blades is governed by the inlet axial velocity and whirl angle at station 2. Some aspects of the performance of the rotor can therefore be understood in terms of the inlet whirl angle and axial velocity distributions in Figs. 8 and 10. Although the upstream flow redistribution reduces the axial velocity distortion at station 2 compared with that far upstream, the axial velocity distortion at rotor inlet still takes the overall form of a deficit within the 60 deg distorted sector.

Low axial velocity and counter-swirl both act to increase the incidence onto the rotor blades compared with the design condition, while co-swirl and high axial velocity act to reduce it. Greater turning is imparted to high-incidence flow by the rotor compared with the design condition and the work input into this flow is correspondingly increased. The opposite applies to low incidence flow, which undergoes less turning and receives lower work input.

The rotor exit stagnation pressure plot in Fig. 11 can be explained in terms of the above arguments. A large region of high stagnation pressure indicates high work input into the low axial velocity and counter-swirling regions of flow. A dark blue region

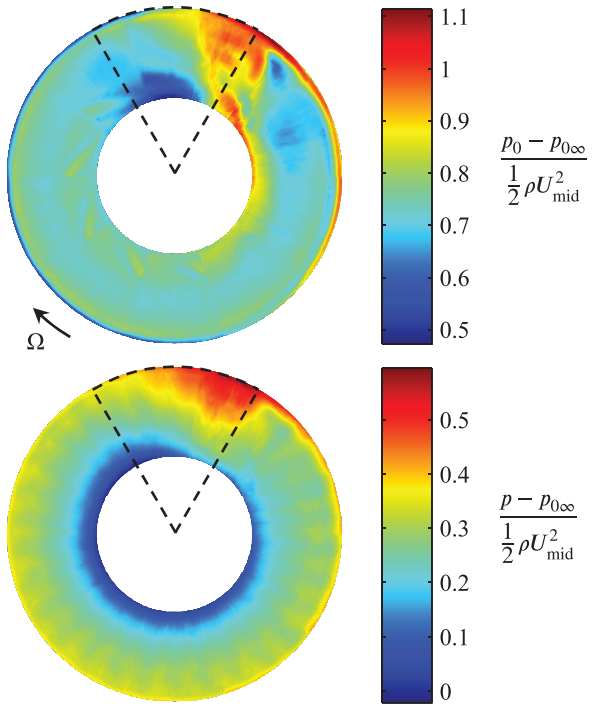


Fig. 11 Contours of stagnation and static pressure at rotor exit (station 3)

of low stagnation pressure corresponds to the intensely co-swirling flow near the hub that lies just outside the distorted sector at rotor inlet. The result is that the stagnation pressure distortion is transferred through the rotor but its shape, location and magnitude are altered. Indeed, due to the high incidence within the distorted sector, much of the distorted fluid experiences such a high pressure rise through the rotor that it emerges with a stagnation pressure comparable to, or greater than, much of fluid originating from outside the distorted sector.

Figure 10 also shows the extent of the mass flow redistribution that takes place within the rotor itself. High attenuation of the axial velocity distortion is achieved above midspan, while a region of low axial velocity fluid remains near the hub. Another region of low axial velocity fluid at the casing on the counter-swirl side is evidence of a flow separation at the rotor tip that occurs as the rotor leaves the distorted sector. The high turning imparted to the tip flow means that the fluid here receives high work input as well as experiencing a high level of loss and therefore, as shown in Fig. 11, a high stagnation pressure is observed in the separated region. Full recovery of the separation does not take place until the affected blades reach the sector opposite the location of the gauze. This separation indicates that the loading at the rotor tip is increased beyond its high design-point value by the presence of the inlet distortion.

The radial flow observed in the upstream redistribution was also observed at rotor exit; it is evident on the bottom of Fig. 12 with its location and direction shifted by about 17 deg in the direction of rotation of the rotor compared with Fig. 9. This indicates an ongoing redistribution of mass in the radial direction. Its reduced intensity indicates that the rotor acts to suppress it, and its intensity decreases further downstream, as the lower plot in Fig. 11 indicates that it is flowing against the static pressure gradient.

Distortion of the rotor exit whirl angle distribution in and around the original distorted sector is apparent in the upper plot in Fig. 12. This whirl angle is in turn governed by the local axial velocity and by the flow turning imparted by the rotor. Comparison with the axial velocity distribution on the bottom of Fig. 10 indicates that the high whirl angle regions correspond directly to the observed regions of low axial velocity, which cause the flow here

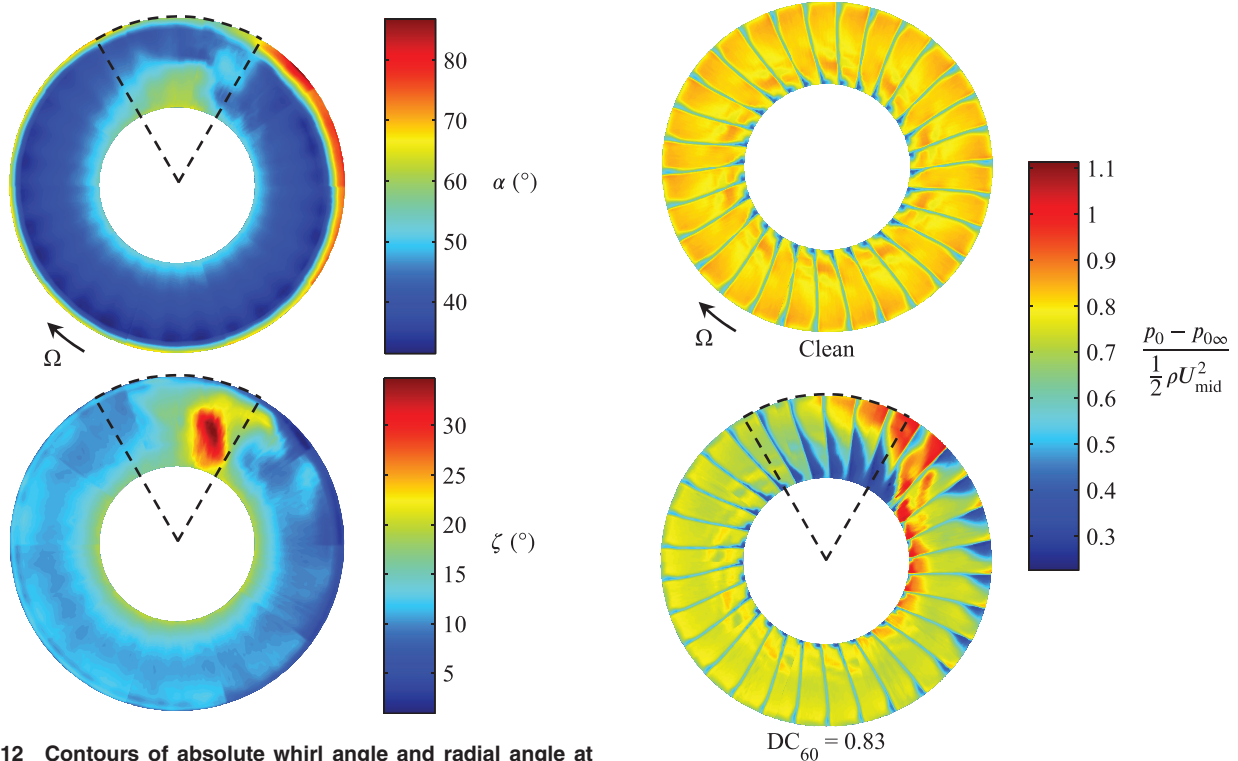


Fig. 12 Contours of absolute whirl angle and radial angle at rotor exit (station 3)

to be overturned in the absolute frame of reference. The extent and magnitude of the whirl angle distortion at rotor exit is therefore directly dependent on the degree of mass flow redistribution that occurs upstream of, and within, the rotor.

The effect of this whirl angle distortion is to present large incidence variations onto the stator blades that lie immediately downstream. The regions of high incidence lead to local flow separations on the suction surfaces of the affected blades. These separations show up as regions of low stagnation pressure on the lower plot in Fig. 13 when compared with the design point in clean flow on the top. In the distorted flow case, corner separations at the hub increase in severity as the distorted sector is approached in the clockwise direction. The wakes away from the endwalls thicken, indicating that profile loss also increases in this region. Within the distorted sector itself, the flow separations extend from the hub to well above midspan. The location of these separations corresponds to the region of high whirl angle, low axial velocity flow extending from the hub at rotor exit. The stator blade separations here therefore depend directly on the extent of the mass flow redistribution that occurs upstream. A similar pattern of stator blade hub separations has been observed in computational calculations of a transonic fan stage subject to inlet distortion [31]. Further clockwise, the hub separation returns to normal just beyond the distorted sector. Tip separations of increasing severity begin to develop instead. A comparison with Fig. 12 indicates that these are caused by the whirl angle distortion due to the flow separation at the rotor tip.

Fan Performance Analysis

Overall Rotor and Stage Performance. A comparison of the overall performance of the rotor and stage between clean and distorted flow is presented in Table 2 in terms of the nondimensional pressure rise, ψ , and the isentropic efficiency, η . The total-to-total and total-to-static pressure rise values were nondimensionalized using a dynamic head based on the midspan blade speed,

$$\psi_{tt} = \frac{p_{0*} - p_{02}}{\frac{1}{2}\rho U_{mid}^2} \quad \psi_{ts} = \frac{p_4 - p_{02}}{\frac{1}{2}\rho U_{mid}^2} \quad (2)$$

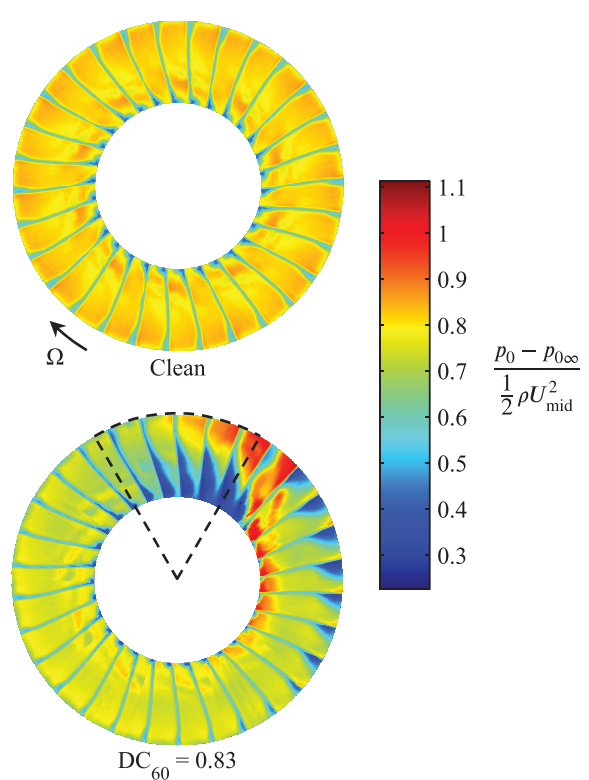


Fig. 13 Contours of stagnation pressure at stator exit (station 4) in clean and distorted flow

For the case of ψ_{tt} , p_{0*} could refer to either p_{03} or p_{04} to give a rotor or stage parameter, respectively. The difference between the two represents the stagnation pressure loss across the stator row. An expression for η follows from the definition of isentropic efficiency for a compressor stage,

$$\eta_{tt} = \frac{(h_{0*} - h_{02})_s}{h_{03} - h_{02}} \quad \eta_{ts} = \frac{(h_4 - h_{02})_s}{h_{03} - h_{02}} \quad (3)$$

The work input, $(h_{03} - h_{02})$, is related to the change in angular momentum of the flow through the rotor and to the rotor shaft speed by Euler's work equation. For incompressible flow, the isentropic work input to the fan is related to the change in stagnation pressure by $\Delta h_{0,s} = \Delta p_0/\rho$. The following expressions were therefore used to calculate the efficiency from the area traverse measurements,

$$\eta_{tt} = \frac{p_{0*} - p_{02}}{\rho\Omega((rV_\theta)_3 - (rV_\theta)_2)} \quad \eta_{ts} = \frac{p_4 - p_{02}}{\rho\Omega((rV_\theta)_3 - (rV_\theta)_2)} \quad (4)$$

All of the flow variables used to calculate these parameters were mass-averaged from the full-annulus results presented above. Cumpsty and Horlock [32] have shown that for low-speed machines a mass average accurately preserves the character of nonuniform flows for the purpose of comparing work exchanges and thrust.

Table 2 Overall performance parameters at $\phi = 0.5$

Parameter	Clean	$DC_{60} = 0.83$
ψ_{tt}	Rotor	0.864
	Stage	0.847
ψ_{ts}	Stage	0.548
η_{tt} (%)	Rotor	92.6
	Stage	90.8
η_{ts} (%)	Stage	59.2
		52.0

The key result from Table 2 is that the inlet distortion caused the stage total-to-total efficiency to decrease by 5.3 percentage points. Out of this decrease, 4.6 percentage points were attributed to reduced rotor efficiency and about 0.7 percentage points to extra loss in the stator row. The effect of the distortion was both to increase the overall work input from the rotor and to decrease the resulting pressure rise, with additional stagnation pressure loss in the stator due to the flow separations caused by the rotor exit whirl angle distortion. Due to the reduced flow uniformity at stator exit and the strong secondary flows associated with the separations, the decrease in η_{ts} was greater than that in η_{tt} , at 7.2 percentage points.

Table 3 presents this comparison in terms of the lost useful work generated in the rotor and stator, normalized by the total rotor work input. Since the flow through the machine is incompressible, changes in T are small and lost work is directly proportional to entropy generation. Table 3 shows that the balance of entropy generation between the fan components is changed by the introduction of the distortion, with the rotor generating a greater proportion of the total entropy change.

Rotor Performance Breakdown. The above results showed that the rotor dominated the overall loss generation in distorted flow and that it experienced a greater drop in performance with the introduction of the distortion. Because of the nonaxisymmetry of the flow and the fact that quantities, such as efficiency, pressure rise, and entropy changes must be evaluated along streamlines or

streamtubes, a further breakdown of the loss sources in the rotor can only be obtained by tracking streamtubes between rotor inlet and rotor exit. Provided that the location of any streamtube at station 3 can be related to its position at station 2, Eqs. (2)–(4) can be applied on a per-streamtube basis to break down the full-annulus performance. An analysis such as this is then able to correctly capture all changes in flow properties across the rotor.

To this end, a simple streamtube tracking calculation was implemented which used the measured experimental data to estimate particle displacements through the rotor. The method was purely kinematic in nature with the emphasis on simplicity and robustness. A summary of the principles of its operation is given in the Appendix.

The boundaries of six streamtubes taking the form of six sectors with equal area were seeded at rotor inlet, as shown on the top of Fig. 14. At rotor inlet, sector 1 contains all of the distorted fluid plus some additional fluid that has arrived in the sector due to the upstream flow redistribution. The streamtube tracking calculation then estimated the locations of these boundaries at rotor exit. These are shown on the bottom of Fig. 14. Table 4 summarizes the performance of the rotor within each of these sectors.

The most striking result from Table 4 is that the rotor achieved its best performance within the distorted sector, with efficiency comparable to its clean flow value. The high pressure rise achieved in this sector indicates the high work input from the rotor into the distorted fluid. It is clear that loss generation in the remaining sectors is the main contributor to reduced rotor

Table 3 Effect of inlet distortion on the lost work generation in the rotor and stator

Lost work parameter	Clean	DC ₆₀ = 0.83	Percentage increase
(TΔs) _{Rotor} (%) $h_{03} - h_{02}$	7.5	12	62
(TΔs) _{Stator} (%) $h_{03} - h_{02}$	1.9	2.5	33

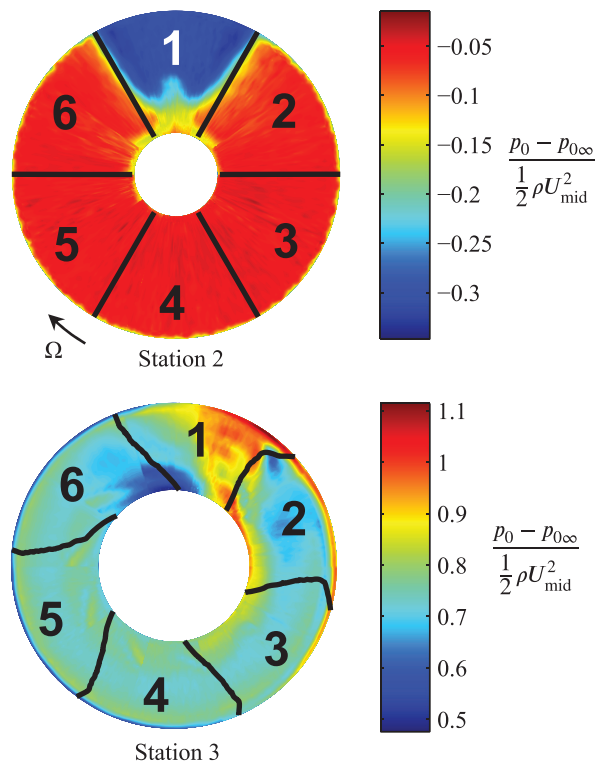


Fig. 14 Six tracked sectors overlaid on contours of stagnation pressure at rotor inlet and exit

Table 4 Rotor performance breakdown for operation with DC₆₀ = 0.83 distortion

Sector	ϕ	$\psi_{tt} - \psi_{tt,Clean}$	$\eta_{tt} - \eta_{tt,Clean}$
1	0.35	0.260	0.0
2	0.50	-0.031	-13
3	0.52	-0.055	-7.3
4	0.54	-0.054	-1.1
5	0.54	-0.044	-2.0
6	0.53	-0.067	-3.5
Overall	0.50	-0.014	-4.6

performance. Despite the localized nature of the distortion, the rotor is detrimentally affected throughout the annulus. Figure 15, which compares the loss generation in each sector to the baseline clean flow value, confirms this picture. A dramatic increase in loss occurs in sectors 2 and 3 as the rotor leaves the distorted sector and recovery to the clean flow value is never achieved outside of the distorted sector. Table 4 and Fig. 15 therefore show that the additional loss generation within the fan stage in distorted flow is dominated by the performance of the rotor in sectors 2–6.

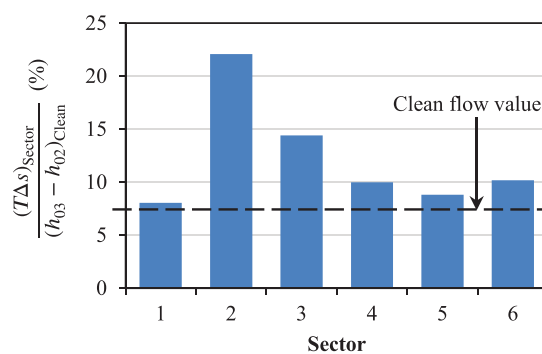


Fig. 15 Breakdown of lost work generation in the rotor with DC₆₀ = 0.83 distortion

Table 4 shows that the mass flow rates through these sectors are above the design value, with ϕ exceeding 0.5, in order to compensate for the reduced mass flow rate through the distorted sector. Consequently, the axial velocity in these sectors is above the design value. In addition, whirl angle distortion created by the upstream flow redistribution is present throughout these sectors. Both of these effects are shown in Fig. 16. By comparing the axial velocity and absolute whirl angles with their design values, it was possible to estimate the resulting incidence angle onto the rotor blades. The circumferential variation in incidence is also plotted in Fig. 16 and velocity triangles are presented in Fig. 17 for two representative coordinates; one within the distorted sector and one directly opposite the distorted sector.

Within sector 1, high positive incidence is observed due to the axial velocity deficit, as represented in the velocity triangle for coordinate X in Fig. 17. As well as the highly three-dimensional nature of the flow in sector 1, shown in Figs. 6–9, the steepness of the gradients in the incidence plot highlights the fact that unsteady phenomena will play an important role in the rotor's performance here. As a rotor blade moves from sector 6 into sector 1, the incidence angle onto the sections near the hub increases by almost 20 deg within the circumferential distance of a single rotor blade passage (18 deg).

Outside sector 1, the high axial velocity reduces the incidence onto the rotor blades. In areas where the flow is co-swirling, this effect is exacerbated, while the opposite occurs in counter-swirling regions. In sectors 4–6, the rotor therefore tends to

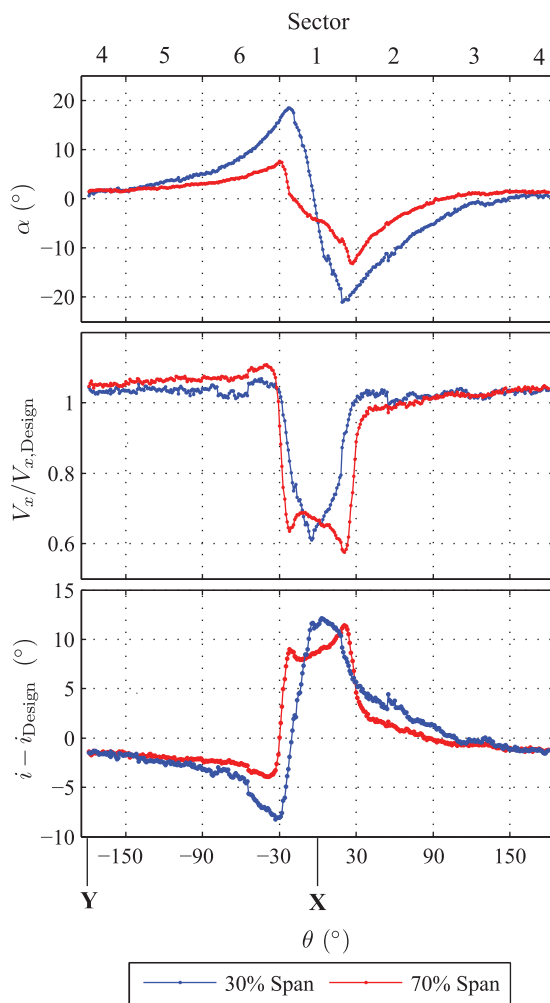


Fig. 16 Absolute whirl angle, axial velocity and incidence variations at rotor inlet (station 2) in distorted flow. Incidence was defined positive for flow onto the pressure surface.

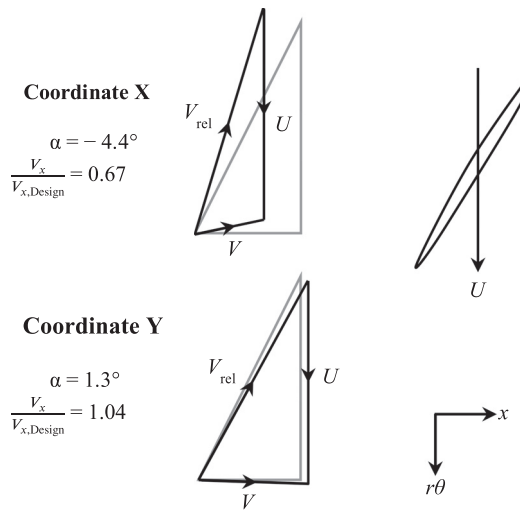


Fig. 17 Examples of two rotor inlet velocity triangles in distorted flow at 70% span compared with the design condition (shown in gray)

operate at negative incidence, shifting it off the design point shown on Fig. 5. The reductions in pressure rise and efficiency in Table 4 occur as a consequence. The velocity triangle for coordinate Y in Fig. 17 demonstrates the fact that the rotor operates at an off-design condition even when it is directly opposite the location of the original inlet distortion. The rotor appears to respond to the conditions in these sectors in a quasi-steady fashion, with efficiency decreasing from 4 to 6 as the incidence becomes more negative.

The severity of the flow separation at the rotor tip in sectors 2 and 3 contributes to the high level of loss here. The incidence variation at 70% span in Fig. 16 reveals that the peak positive incidence value near the tip is encountered at $\theta = 22$ deg, immediately before the rotor leaves the distorted sector. This agrees well with the observed initial location of the tip flow separation in Figs. 10 and 12. In addition, the rotor continues to operate at positive incidence immediately after leaving the distorted sector due to the counter-swirl upstream, further affecting its performance in sectors 2 and 3.

Figure 16 shows that for a given span fraction, the design incidence value occurs at only two circumferential coordinates where $(i - i_{\text{Design}})$ passes through zero. Due to the asymmetry of the flow, the location of these circumferential coordinates depends on the local span fraction. Therefore, despite the localized nature of the inlet distortion, at no point in the annulus does the rotor operate at its design condition. The resulting full-annulus reduction in rotor performance is the dominant cause of the observed reduction in fan efficiency under operation with inlet distortion and it is a key challenge that must be overcome to achieve improved aerodynamic performance in BLI fans.

Conclusions

High spatial resolution measurements have been used to observe the flow field and loss sources within a low-speed fan stage operating with a continuous single-sector inlet stagnation pressure distortion.

When inlet distortion is present, a redistribution of mass is induced upstream of the rotor in response to the asymmetric flow field. The resulting flow is highly three-dimensional and interacts strongly with the fan spinner and hub. In the test case considered, a 50% increase in mass flow rate in the distorted sector was observed between the distortion input and the rotor leading edge and the redistribution was identified as being of key importance to the performance and stability of the fan.

Reductions in rotor and stage total-to-total efficiency of 4.6 and 5.3 percentage points, respectively, were observed in operation with inlet distortion compared with the design point. The additional loss generation was dominated by the contribution from the rotor and had the following specific causes:

- (i) The mass flow asymmetry and upstream flow redistribution led to variations in axial velocity and whirl angle at rotor inlet. The incidence angle seen by the rotor therefore varied circumferentially and radially, causing the rotor to operate at varying off-design conditions. This effect occurred throughout the annulus and the additional loss was generated throughout the annulus, despite the localized nature of the inlet distortion.
- (ii) A substantial flow separation was observed at the rotor tip, caused by exacerbation of the high tip loading by high-incidence flow encountered as the rotor leaves the distorted sector.
- (iii) Regions of separated flow extended from the hub to beyond midspan in the portion of the stator row immediately downstream of the distorted sector. These were caused by whirl angle distortion at rotor exit and were shown to depend directly on the upstream mass flow redistribution. Additionally, the upstream separation of the flow over the rotor tip led to a corresponding region of distorted whirl angle which separated the tip flow over the downstream stators.

The understanding of fan-distortion interaction and loss sources developed in this paper can be used as a basis for further research into the performance of fans operating with representative inlet boundary layer profiles. With such research it should be possible to determine the design changes required to improve the performance of practical BLI fan systems.

Acknowledgment

The authors are grateful to EPSRC for funding the work in this paper through Grant No. EP/F015070/1. The aerodynamic and overall design of the rig was carried out by Chris Freeman and Ivor Day, who are also gratefully acknowledged for their input into explaining the background to its resulting performance. Neil Houghton, Alistair Ross, and Barney Coles are acknowledged for their roles in implementing the detailed mechanical design and construction of the rig. Many thanks are also due to Colin Bullman for his rapid response in rectifying all issues encountered with the operation of the rig. Technical advice relating to the work from experts at Rolls-Royce plc is also gratefully acknowledged.

Nomenclature

Symbols

- h = enthalpy
- i = incidence angle
- p = pressure
- r = radial coordinate
- s = entropy
- T = temperature
- U = rotor blade speed
- V = velocity
- x = axial coordinate
- α = absolute whirl flow angle
- β = relative whirl flow angle
- ζ = radial flow angle
- η = isentropic efficiency
- Ω = rotor shaft speed
- θ = circumferential coordinate
- ρ = density
- ϕ = flow coefficient
- ψ = pressure rise coefficient

Abbreviations

- BLI = boundary layer ingestion
- DC₆₀ = distortion index based on a 60 deg sector
- LE = leading edge
- TE = trailing edge

Subscripts

- 0 = stagnation quantity
- 1 = value upstream of spinner
- 2 = value at rotor inlet
- 3 = value at rotor exit
- 4 = value at stator exit
- mid = value at midspan
- rel = relative frame quantity
- s = isentropic process
- ts = total-to-static parameter
- tt = total-to-total parameter
- x = axial component
- ∞ = value well upstream of inlet
- θ = circumferential component

Appendix: Streamtube Tracking Method

The inputs to the streamtube tracking routine were the locations of the boundaries of six sectors at station 2, the geometric definition of the rig and the experimental data at stations 2 and 3. Its objective was to calculate the locations of the boundaries of the six sectors at station 3. This task was reduced to the estimation of the radial and circumferential components of particle displacements between these stations, with the axial component fixed by the distance between the stations.

The true particle path in the meridional plane, indicated on Fig. 18, could be approximated as two straight line segments. The particle was assumed to travel at an angle of ζ_2 until reaching the midpoint of x_2 and x_3 and then to travel at an angle of ζ_3 until reaching station 3. Knowledge of $x_3 - x_2$ then allowed the radial displacement, $\Delta r_{2 \rightarrow 3}$, to be estimated. This calculation was solved iteratively, as the value of ζ_3 depends on the final location of the particle.

The circumferential component of displacement was further broken down into the relative frame motion of a particle through a rotor blade passage and the absolute component of displacement due to the rotation of the rotor, as shown in Fig. 19. The former involved a similar calculation to the radial component but used the relative whirl flow angles, β , instead of ζ . The latter made use of the fact that the measured values of axial velocity at 2 and 3, together with the known axial chord variation along the rotor span, could provide an estimate of the residence time of the particle within the blade passage, t_{res} . Multiplying this by the average

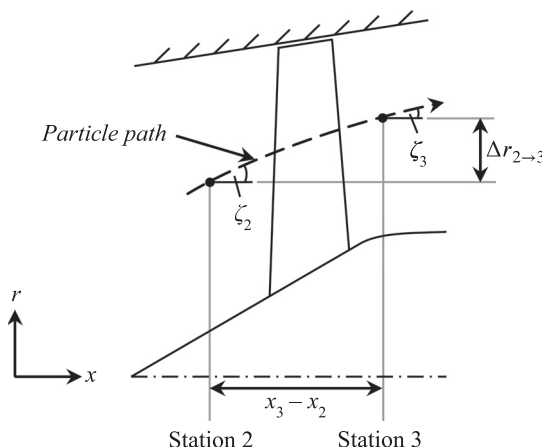


Fig. 18 Meridional view of the rotor showing the data used in the kinematic estimate of radial particle displacement

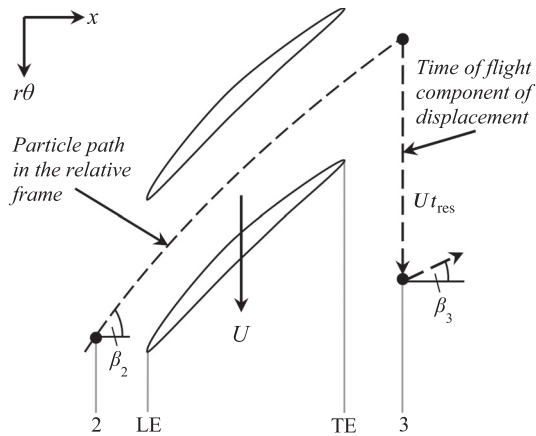


Fig. 19 Cut along a blade-to-blade stream surface showing the kinematic estimate of circumferential particle displacement

blade speed seen by the particle, U , gave an estimate of the time of flight component of displacement. The overall circumferential calculation was solved iteratively together with the radial calculation.

Although the simplicity of this algorithm meant it was unable to capture the complex fluid mechanics of the radial flow within the distorted sector, this problem was circumvented by tracking particles at the boundaries of the distorted sector. It was found that the predicted particle locations at rotor exit were insensitive to small perturbations of the inlet boundaries. The rotor performance calculations performed on the sectors were also insensitive to deliberate perturbation of the boundaries at rotor exit, giving confidence that the trends and conclusions presented in the rotor performance breakdown analysis were valid.

References

- [1] Smith, L. H., 1993, "Wake Ingestion Propulsion Benefit," *J. Propul. Power*, **9**(1), pp. 74–82.
- [2] Kawai, R. T., Friedman, D. M., and Serrano, L., 2006, "Blended Wing Body (BWB) Boundary Layer Ingestion (BLI) Inlet Configuration and System Studies," NASA Contract Report CR-2006-214534.
- [3] Hall, C. A., and Crichton, D., 2007, "Engine Design Studies for a Silent Aircraft," *ASME J. Turbomach.*, **129**(3), pp. 479–487.
- [4] Hall, C. A., Schwartz, E., and Hileman, J. I., 2009, "Assessment of Technologies for the Silent Aircraft Initiative," *J. Propul. Power*, **25**(6), pp. 1153–1162.
- [5] MIT, Aurora Flight Sciences, and Pratt & Whitney, 2010, "N+3 Aircraft Concept Designs and Trade Studies, Final Report," NASA Contract Report CR-2010-216794.
- [6] Felder, J. L., Kim, H. D., and Brown, G. V., 2009, "Turboelectric Distributed Propulsion Engine Cycle Analysis for Hybrid Wing Body Aircraft," 47th AIAA Aerospace Sciences Meeting, Orlando, FL, January 5–8, Paper No. AIAA 2009-1132.
- [7] Felder, J. L., Brown, G. V., Kim, H. D., and Chu, J., 2011, "Turboelectric Distributed Propulsion in a Hybrid Wing Body Aircraft," 20th ISABE Conference, Gothenburg, Sweden, September 12–16, Paper No. ISABE-2011-1340.
- [8] Plas, A. P., Sargeant, M. A., Madani, V., Crichton, D., Greitzer, E. M., Hynes, T. P., and Hall, C. A., 2007, "Performance of a Boundary Layer Ingesting (BLI) Propulsion System," 45th AIAA Aerospace Sciences Meeting and Exhibit, Reno, NV, January 8–11, Paper No. AIAA 2007-450.
- [9] Gorton, S. A., Owens, L. R., Jenkins, L. N., Allan, B. G., and Schuster, E. P., 2004, "Active Flow Control on a Boundary-Layer-Ingesting Inlet," 42nd AIAA Aerospace Sciences Meeting and Exhibit, Reno, NV, January 5–8, AIAA-2004-1203.
- [10] Owens, L. R., Allan, B. G., and Gorton, S. A., 2006, "Boundary-Layer-Ingesting Inlet Flow Control," 44th AIAA Aerospace Sciences Meeting and Exhibit, Reno, NV, January 9–12, AIAA 2006-839.
- [11] Allan, B. G., Owens, L. R., and Lin, J. C., 2006, "Optimal Design of Passive Flow Control for a Boundary-Layer-Ingesting Offset Inlet Using Design-of-Experiments," 44th AIAA Aerospace Sciences Meeting and Exhibit, Reno, NV, January 9–12, AIAA 2006-1049.
- [12] Liou, M.-S., and Lee, B. J., 2012, "Minimizing Inlet Distortion for Hybrid Wing Body Aircraft," *ASME J. Turbomach.*, **134**(3), p. 031020.
- [13] Williams, D. D., 1987, "Review of Current Knowledge of Engine Response to Distorted Inflow Conditions," AGARD CP-400, Engine Response to Distorted Inflow Conditions, Munich, September 8–9, pp. 1-1–1-32.
- [14] Longley, J. P., and Greitzer, E. M., 1992, "Inlet Distortion Effects in Aircraft Propulsion System Integration," AGARD LS-183, Steady and Transient Performance Prediction of Gas Turbine Engines, pp. 6-1–6-18.
- [15] Hynes, T. P., and Greitzer, E. M., 1987, "A Method for Assessing Effects of Circumferential Flow Distortion on Compressor Stability," *ASME J. Turbomach.*, **109**(3), pp. 371–379.
- [16] SAE, 1999, "Inlet Total-Pressure-Distortion Considerations for Gas-Turbine Engines," Standard No. AIR1419 Revision A.
- [17] Greitzer, E. M., and Griswold, H. R., 1976, "Compressor-Diffuser Interaction With Circumferential Flow Distortion," *J. Mech. Eng. Sci.*, **18**(1), pp. 25–38.
- [18] Greitzer, E. M., Mazzawy, R. S., and Fulkerson, D. A., 1978, "Flow Field Coupling Between Compression System Components in Asymmetric Flow," *ASME J. Eng. Power*, **100**(1), pp. 66–72.
- [19] Yao, J., Gorrell, S. E., and Wadia, A. R., 2010, "High-Fidelity Numerical Analysis of Per-Rev-Type Inlet Distortion Transfer in Multistage Fans—Part I: Simulations With Selected Blade Rows," *ASME J. Turbomach.*, **132**(4), p. 041014.
- [20] Yao, J., Gorrell, S. E., and Wadia, A. R., 2010, "High-Fidelity Numerical Analysis of Per-Rev-Type Inlet Distortion Transfer in Multistage Fans—Part II: Entire Component Simulation and Investigation," *ASME J. Turbomach.*, **132**(4), p. 041015.
- [21] Jerez Fidalgo, V., Hall, C. A., and Colin, Y., 2012, "A Study of Fan-Distortion Interaction Within the NASA Rotor 67 Transonic Stage," *ASME J. Turbomach.*, **134**(5), p. 051011.
- [22] Stocks, C. P., and Bissinger, N. C., 1981, "The Design and Development of the Tornado Air Engine Intake," AGARD CP-301, Aerodynamics of Power Plant Installation, Toulouse, France, May 11–14, pp. 10-1–10-21.
- [23] Flitcroft, J. E., Dunham, J., and Abbott, W. A., 1986, "Transmission of Inlet Distortion Through a Fan," AGARD CP-400, Engine Response to Distorted Inflow Conditions, Munich, September 8–9, pp. 13-1–13-11.
- [24] Williams, J. G., Steenken, W. G., and Yuhas, A. J., 1996, "Estimating Engine Airflow in Gas-Turbine Powered Aircraft With Clean and Distorted Inlet Flows," NASA Contract Report No. CR-1996-198052.
- [25] Walsh, K. R., Yuhas, A. J., Williams, J. G., and Steenken, W. G., 1997, "Inlet Distortion for an F/A-18A Aircraft During Steady Aerodynamic Conditions up to 60 deg Angle of Attack," NASA Technical Memorandum No. TM-104329.
- [26] Govardhan, M., and Viswanath, K., 1997, "Investigations on an Axial Flow Fan Stage Subjected to Circumferential Inlet Flow Distortion and Swirl," *J. Therm. Sci.*, **6**(4), pp. 241–250.
- [27] Wadia, A. R., 2011, "Experimental Investigation of a Forward Swept Rotor in a Multistage Fan With Inlet Distortion," *Int. J. Aerospace Eng.*, **2011**(1), p. 941872.
- [28] Strazisar, A. J., Wood, J. R., Hathaway, M. D., and Suder, K. L., 1989, "Laser Anemometer Measurements in a Transonic Axial-Flow Fan Rotor," NASA Technical Paper No. 2879.
- [29] Treaster, A. L., and Yocom, A. M., 1979, "The Calibration and Application of Five-Hole Probes," *ISA Trans.*, **18**(3), pp. 23–34.
- [30] Reid, C., 1969, "The Response of Axial Flow Compressors to Intake Flow Distortion," Proceedings of the Gas Turbine Products and Conference Show, Cleveland, OH, ASME Paper No. 69-GT-29.
- [31] Sun, P., Zhong, J., and Feng, G., 2007, "Flow Field Analysis of Inlet Distortion in a Transonic Fan With Straight and Bowed Stator Blade," Proceedings of ASME Turbo Expo 2007, Montreal, Canada, May 14–17, ASME Paper No. GT2007-27607.
- [32] Cumpsty, N. A., and Horlock, J. H., 2006, "Averaging Nonuniform Flow for a Purpose," *ASME J. Turbomach.*, **128**(1), pp. 120–129.